



## Hematite photoanodes with size-controlled nanoparticles for enhanced photoelectrochemical water oxidation



Amira Y. Ahmed<sup>a</sup>, Mahmoud G. Ahmed<sup>a</sup>, Tarek A. Kandiel<sup>a,b,\*</sup>

<sup>a</sup> Department of Chemistry, Faculty of Science, Sohag University, Sohag 82524, Egypt

<sup>b</sup> Department of Chemistry, King Fahd University of Petroleum & Minerals (KFUPM), Dhahran 31261, Saudi Arabia

### ARTICLE INFO

#### Keywords:

Hematite photoanodes  
Photoelectrochemical water splitting  
Solar hydrogen production  
Morphology directing agents  
IMPS and PEIS

### ABSTRACT

The synthesis of hematite photoanodes with size-controlled nanoparticles is challenging due to the difficulty in finding the appropriate morphology-directing agents. In this paper,  $\text{Ba}^{2+}$  and  $\text{Sr}^{2+}$  ions were successfully employed to synthesize hematite photoanodes with size-controlled nanoparticles using a facile chemical bath deposition method. The synthesized electrodes were characterized by X-ray diffraction (XRD), scanning electron microscopy (SEM), inductively coupled plasma-optical emission spectrometry (ICP-OES), (photo)electrochemical impedance spectroscopy (PEIS), X-ray photoelectron spectroscopy (XPS) and intensity modulated photocurrent spectroscopy (IMPS) measurements. It was found that the average diameter of hematite nanoparticles is decreased by a factor of 13% and 35% by the addition of  $\text{Ba}^{2+}$  and  $\text{Sr}^{2+}$  ions into the chemical bath, respectively. In agreement with these results, the electroactive surface area of Ba- and Sr-modified hematite electrodes increased by 2.4 and 3.2 times, respectively, in comparison with that of bare hematite. The photoelectrochemical measurements under the standard illumination conditions revealed that the generated photocurrent at 1.23 V vs. RHE on Ba- and Sr-modified hematite photoanodes is 2.6 and 3 times higher than that of bare hematite, respectively. Moreover, the photocurrent onset potential for water oxidation on Ba- and Sr-modified hematite photoanodes was shifted cathodically by about 150 and 220 mV, respectively. Based on these results, a good correlation between the photocurrent and the electroactive surface area was observed at high bias potential (i.e., 1.23 V vs. RHE) evincing that the photocurrent enhancement can be readily attributed to the enhanced electroactive surface area. The cathodic shift in the photocurrent onset potential of water oxidation was elucidated, however, by the higher density of surface states and the higher rate constant of charge transfer as proven by the PEIS and IMPS measurements, respectively.

### 1. Introduction

Producing hydrogen gas as a clean-burning chemical fuel by using photoelectrochemical cells has recently attracted great attention [1]. This approach, however, is still elusive until discovering efficient, stable, and scalable photoactive materials for photoelectrochemical water splitting. Up to date, many materials have been investigated either as photoanodes (e.g.,  $\text{TiO}_2$  [2],  $\text{BiVO}_4$  [3],  $\text{WO}_3$  [4],  $\text{Bi}_2\text{WO}_6$  [5],  $\text{TaON}$  [6], and  $\text{BaTaO}_2\text{N}$  [7]) or as photocathodes (e.g.,  $\text{Cu}_2\text{O}/\text{NiO}_x$  [8], and  $\text{CaFe}_2\text{O}_4$  [9]). Among these materials, hematite ( $\alpha\text{-Fe}_2\text{O}_3$ ) has attracted extensive interest due to its narrow band gap, availability, non-toxicity, and the ease of its fabrication in large scale. Hematite, however, suffers from some hitches, which hinder its practical application. These include: (i) low absorption coefficient [10], (ii) poor carrier conductivity (high resistance) [11], (iii) the short life time and diffusion length of photogenerated charge carriers [12], and (iv) sluggish kinetic

of water oxidation on its surface [10].

To overcome these constraints, several strategies have been employed. For example, the incorporation of either p-type ( $\text{Mg}^{2+}$ ,  $\text{Zn}^{2+}$ ) [13,14], n-type dopants ( $\text{Si}^{4+}$ ,  $\text{Ti}^{4+}$ ,  $\text{Sn}^{4+}$ ,  $\text{Zr}^{4+}$ ) [15–18], or nonmetal elements (Se, N, S) [19–21] in hematite has been found to increase the charge carriers density and thus to enhance the carriers conductivity. Nano-engineering of hematite photoanodes via different pathways including surface modification, introducing an underlayer, and controlling the morphologies has also been found to be an effective strategy to enhance the efficiency. For instance, the modification of photoelectrode/liquid interface with passivation layer and/or oxygen evolution catalyst has been successfully employed to reduce the surface recombination and to enhance the charge transfer efficiency at the photoelectrode/liquid interface [22–24]. The charge separation efficiency has also been improved by the formation of heterojunctions [25,26], composites [27], and the introduction of electron collecting scaffolds

\* Corresponding author at: Department of Chemistry, King Fahd University of Petroleum & Minerals; Department of Chemistry, Faculty of Science, Sohag University.  
E-mail addresses: [tarek.kandiel@kfupm.edu.sa](mailto:tarek.kandiel@kfupm.edu.sa), [kandiel@science.sohag.edu.eg](mailto:kandiel@science.sohag.edu.eg) (T.A. Kandiel).

[28]. In our recent work, we developed a facile method for the fabrication of p-CaFe<sub>2</sub>O<sub>4</sub>/n-Fe<sub>2</sub>O<sub>3</sub> heterojunction photoanode with enhanced photoactivity by adding Ca<sup>2+</sup> ions into an aqueous based chemical bath which contains FeCl<sub>3</sub> followed by two step annealing process [26]. Ding et al. improved both charge separation and injection by the creation of electron transfer layer from Li ions between hematite and conducting substrate [29]. An attempt to use Ba and Sr instead of Li resulted in the reduction of the generated photocurrent and thus lowered the overall efficiency [29].

It was previously reported that the modification of photocatalyst (e.g. NaTaO<sub>3</sub>) and/or photoelectrode (e.g. Ta<sub>3</sub>N<sub>5</sub>) with Ca, Sr and Ba significantly influence the photoactivity [30,31]. This was attributed to the formation of fine particles and to the construction of surface nanostep [30]. Moreover, it was also reported that hematite crystals with different morphologies could be synthesized in the presence of Ca<sup>2+</sup>, Sr<sup>2+</sup>, and Ba<sup>2+</sup> ions through an ion-assisted growth route under hydrothermal conditions [32]. Compared to bulk materials, the nanosstructured hematite photoanode with fine particles is highly expected to exhibit higher activity owing to its high surface-to-volume ratio and to the presence of a higher number of active surface sites. These reports and facts motivated us to investigate the effect of Ba<sup>2+</sup> and Sr<sup>2+</sup> ions existence in the chemical bath during the fabrication of hematite films. Interestingly, it was found that the modification of hematite photoanodes by adding Ba<sup>2+</sup> and Sr<sup>2+</sup> ions into the chemical bath enhances the photocurrent at 1.23 V vs. RHE by a factor of 2.6 and 3 times, respectively, in comparison to that of bare hematite. Moreover, the photocurrent onset potential for water oxidation on Ba- and Sr-modified hematite photoanodes has been cathodically shifted by about 150 and 220 mV, respectively, relative to that on bare hematite measured at 0.01 mA cm<sup>-2</sup>. The improved photoactivity of Ba- and Sr-modified hematite photoanodes has been explored by measuring the electroactive surface area, the density of surface states, and the rate constants of charge carriers transfer and recombination using cyclic voltammetry, (photo)electrochemical impedance spectroscopy ((P)EIS), and intensity modulated photocurrent spectroscopy (IMPS) techniques, respectively.

## 2. Experimental

### 2.1. Synthesis

Bare hematite, Ba-, and Sr-modified hematite films were prepared by a simple template-less film processing technique as previously reported [26]. Briefly, fluorine doped tin oxide coated glass (FTO, 1 × 1.5 cm<sup>2</sup>, Sigma-Aldrich, TEC 7, surface resistivity ~7 Ω/sq, thickness 2.2 mm) were cleaned with detergent, acetone, ethanol, and water, respectively, using an ultrasonic bath. Subsequently, the FTO substrates were vertically placed in a glass vessel, which contains 0.75 mmol of FeCl<sub>3</sub>·6H<sub>2</sub>O (Sigma-Aldrich) dissolved in bi-distilled water and the desired amount of BaCl<sub>2</sub>·2H<sub>2</sub>O or SrCl<sub>2</sub>·6H<sub>2</sub>O. The final volume was 5 mL and the concentration of Ba<sup>2+</sup> an Sr<sup>2+</sup> ions was adjusted to be 1, 2, or 3 at.%. The glass vessel was sealed and placed in an oven pre-adjusted to 95 °C for 6 h. After natural cooling, the grown uniform yellow layers on the FTO substrates were rinsed in water to remove the excess inorganic salts. The films were then dried in air and heat-treated at 550 °C for 60 min and at 800 °C for 20 min. For the preparation of bare hematite films, the same procedure was used without adding Ba<sup>2+</sup> and Sr<sup>2+</sup> ions into the chemical bath. To illustrate the effect of the short-time annealing at 800 °C on the conductivity of the FTO substrate, Nyquist plots for bare hematite films heat-treated at 550 and 800 °C were measured and presented in Fig. S1 as an example. It was found that the films annealed at 550 and 800 °C exhibit almost the same impedance indicating that the heat-treatment at 800 °C for 20 min does not destroy the conductive FTO layer.

Photoelectrodes were fabricated by connecting copper wires to the FTO substrates, coated with the bare and modified hematite films, from the conductive side using silver paste. The active area was then

confined to be 0.5 cm<sup>2</sup> by using non-conductive epoxy resin.

### 2.2. Characterization

The bare hematite, Ba-, and Sr-modified hematite films were characterized by x-ray diffraction (XRD) and scanning electron microscopy (SEM) using Bruker D8 advance diffractometer and Nova Nano 630 scanning electron microscope (FEI Company), respectively. An AMICUS/ESCA 3400 KRATOS instrument equipped with Mg-anode operated at 12 kV and 10 mA was used for the X-ray photoelectron spectroscopy (XPS) analysis. The XPS spectra were calibrated using the C 1s peak located at 284.6 eV as a reference. The composition of bare hematite and Ba- and Sr-modified hematite films was analyzed using PlasmaQuant® PQ 9000 inductively coupled plasma-optical emission spectrometer (ICP-OES, Analytik Jena AG). Aqua-regia was employed in the digestion step. The thickness of the films was determined by using Talysurf profilometer (Taylor Hobson).

### 2.3. Photoelectrochemical measurements

The photoelectrochemical measurements were performed using an Autolab PGSTAT302N potentiostat. The simulated solar light source was a Xenon lamp (Osram XBO 70 W) in a Müller LXH 100 lamp housing coupled with condenser with aspheric lens and an AM 1.5 G filter (Sciencetech Inc.). A digital handheld energy meter (Thorlab, PM100D) connected with a calibrated high-sensitivity thermal sensor (S401C, Thorlabs) was used to adjust the light intensity to be 1 sun (100 mW cm<sup>-2</sup>). A teflon-made cell adapted with a quartz window on one side for illumination was employed for the photoelectrochemical measurements. An aqueous solution of NaOH (1.0 M), a platinum wire, and a Hg/HgO (1.0 M NaOH) electrode were used as an electrolyte, a counter electrode, and a reference electrode, respectively. The measured potentials vs. Hg/HgO were converted to the reversible hydrogen electrode (RHE) scale according to the Nernst equation: E<sub>RHE</sub> = E<sub>Hg/HgO</sub> + 0.059 pH + E<sub>Hg/HgO</sub>, where E<sub>RHE</sub> is the converted potential vs. RHE, E<sub>Hg/HgO</sub> = 0.098 V at 25 °C, and E<sub>Hg/HgO</sub> is the experimentally measured potential against Hg/HgO reference [33].

### 2.4. IMPS measurements

IMPS responses were measured using a photoelectrochemical workstation consisting of an Autolab PGSTAT302N potentiostat adapted with a triple LED array (470 nm), DAC164 and FRA32M modules to control the DC and AC output of the LED Driver, respectively. NOVA 2.1 software was used to control the potentiostat and collect the data. The IMPS responses were examined at a frequency ranging from 0.1 Hz to 10 kHz at different applied potential, i.e., 0.7–1.3 V vs. RHE at 0.1 intervals. The AC amplitude was taken as 10% of the DC output and the light intensity of the LED array at the electrode surface was 52.0 mW cm<sup>-2</sup>.

### 2.5. EIS measurements

Nyquist plots were measured at different applied potential in the frequency range from 100 kHz to 0.1 Hz at an amplitude frequency of 10 mV under standard illumination conditions. Mott-Schottky (M-S) plot was examined in the dark at 1.0 kHz in the potential window from 0.4 to 1.4 V vs. RHE.

## 3. Result and discussions

### 3.1. Characterization

Fig. 1 shows the XRD patterns of bare hematite, Ba- and Sr-modified hematite films. Two peaks located at 35.7° and 64.0° (2θ) are observed in all films. These peaks can be assigned to the (110) and (300)

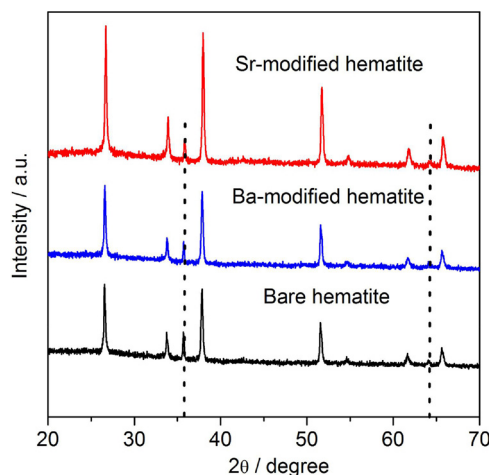


**Fig. 1.** XRD patterns of bare hematite and of Ba- and Sr-modified hematite films. The vertical lines indicate Bragg positions for hematite according to the JCPDS No. 033-0664. The other peaks indicate Bragg positions for FTO according to the JCPDS No. 041-1445.

diffractions of hematite hexagonal phase, respectively, according to the JCPDS card no. 033-0664. All other diffraction peaks observed in the XRD patterns can readily be referred to the tin oxide film on the conductive glass according to the JCPDS card no. 041-1445 indicating the stability of the FTO layer after short-time heat-treatment at 800 °C. Neither characteristic peaks for Ba and Sr oxides nor for other iron oxide structures are detected evidencing the successful conversion of the as-prepared FeOOH into hematite structure in the presence of Ba<sup>2+</sup> and Sr<sup>2+</sup> ions. It was also observed that the intensity of (110) diffraction peak is higher than that of (300) diffraction peak indicating the preferential growth of hematite particles in the [110] direction [34]. In addition, no shifting in the position of the diffraction peaks of hematite is observed after the modification with Ba or Sr. This indicates that under our conditions, the Ba<sup>2+</sup> and Sr<sup>2+</sup> ions do not substitute for the Fe<sup>3+</sup> in the hematite lattice and more likely the doping of hematite with Ba or Sr does not occur. This can be understood by considering that the as-prepared FeOOH films have been grown on FTO substrates at low temperature (95 °C) and pressure and at low ripening process. In fact, the ionic radii of Ba<sup>2+</sup> and Sr<sup>2+</sup> are bigger than that of Fe<sup>3+</sup> by a factor of 1.8 and 2.1, respectively, which makes the doping of hematite with Ba<sup>2+</sup> and Sr<sup>2+</sup> ions under the employed condition unreasonable [35]. This conclusion is further supported by XPS, ICP-OES, and EIS analysis as discussed in the next sections.

Fig. 2 shows the SEM images of bare hematite and of Ba- and Sr-modified hematite films. It is apparent from these images that the diameter of the rod-like hematite particles prepared in presence of Ba<sup>2+</sup> and Sr<sup>2+</sup> ions is smaller than that of bare hematite. By analysing the SEM images, the particle size distribution histograms have been constructed (Fig. 2). It can be seen from these histograms that the average diameter of the hematite particles is decreased by a factor of 13% and 35% upon addition of Ba<sup>2+</sup> and Sr<sup>2+</sup> ions into the chemical bath, respectively. This indicates that Ba<sup>2+</sup> and Sr<sup>2+</sup> ions act as morphology-directing agents. This finding agrees with the recent report that alkaline earth metal ions can be employed as morphology-directing agents for the preparation of hematite crystals with different morphologies without employing any surfactants or templates [32]. The decreased diameter of the rod-like particles is expected to facilitate the diffusion of the photogenerated holes to the surface, whereas the preferential growth of hematite particles in the [110] direction is expected to enhance the transfer of the photogenerated electrons to the back contact [36].

To investigate the existence of Ba and Sr in the fabricated hematite films, they have been analyzed by using XPS (Fig. S2). Unlike Ca<sup>2+</sup> ions

in the previous report [26], we were not able to detect Ba and Sr in the investigated films indicating that either their concentration, which might be incorporated into the hematite structure, lies below the detection limit of this technique or they are acting as morphology-directing agents indeed. This finding was further confirmed by the ICP-OES analysis (Table S1). No Ba and Sr ions can be detected further evincing that they act as morphology-directing agents. The amount of Fe<sub>2</sub>O<sub>3</sub> grown on 1.0 cm<sup>2</sup> FTO substrate was calculated to be 23.4, 22.7, and 22.8 µg per 1.0 cm<sup>2</sup> for bare hematite, Ba- and Sr-modified hematite films, respectively, indicating that they have almost the same film thickness. This result was further confirmed by measuring the film thickness using the profilometer. In good agreement with the ICP-OES results, the thickness of the three films was found to be almost the same and it lies in the range of 67 ± 20 nm.

### 3.2. Photoelectrochemical and electrochemical measurements

The photoelectrochemical responses for hematite photoanodes prepared in the presence of different concentrations of Ba<sup>2+</sup> or Sr<sup>2+</sup> ions (i.e., 1, 2, and 3.0 at.%) have been measured and presented in Figs. S3 and S4, respectively. It was found that the hematite photoanodes prepared from chemical bath which contains 2 at.% of either Ba<sup>2+</sup> or Sr<sup>2+</sup> ions exhibit the highest photoelectrochemical activity. For the ease of comparison, Fig. 3 shows the I-V curve recorded for bare hematite and for Ba- and Sr-modified hematite photoanodes measured under standard illumination conditions (i.e., 100 mW cm<sup>-2</sup>, AM 1.5 G). The generated photocurrent at 1.23 V vs. RHE on Ba- and Sr-modified hematite photoanodes was found to be 2.6 and 3 times higher than that of bare hematite, respectively. Moreover, the photocurrent onset potential for water oxidation on Ba- and Sr-modified hematite photoanodes has been cathodically shifted by about 150 and 220 mV, respectively, relative to that on bare hematite measured at 0.01 mA cm<sup>-2</sup>. The enhanced photocurrent can be generally attributed to the enhanced surface area after modification as it can be concluded from the observed fine particles in the SEM images. While the shift in the photocurrent onset potential for water oxidation can either be attributed to the shift in the flat-band potential [37], or to the charging of the surface states under illumination [38]. To investigate these hypotheses experimentally, the electroactive surface area, the flat-band potential, and the density of the surface states have been measured as described in details below.

The electroactive surface area of bare hematite and of Ba-, and Sr-modified hematite electrodes were calculated electrochemically using the well-established Randles-Sevcik equation:  $I_p = 2.69 \times 10^5 A D^{1/2} n^{3/2} C \nu^{1/2}$  [39], where  $I_p$  is the peak current (A), A is the electroactive surface area of the electrode (cm<sup>2</sup>), C is the concentration of the electroactive species (mol cm<sup>-3</sup>), n is the number of exchanged electrons, D is the diffusion coefficient (cm<sup>2</sup>s<sup>-1</sup>) and  $\nu$  is the scan rate (V s<sup>-1</sup>). According to this equation, for a diffusion-controlled electrochemical process, the current varies linearly with the square root of the scan rate and the slope is proportional to the electroactive surface area. Figs. S5a-c depict the cyclic voltamograms obtained on bare hematite and on Ba- and Sr-modified hematite electrodes, respectively, from an aqueous solution of 0.1 M KCl in the presence of 0.001 M K<sub>4</sub>[Fe(CN)<sub>6</sub>] as an electro-active species at different scan rates. A linear relation between the peak current and the square root of the scan rate has been observed as shown in Fig. 4. Non-zero intercept has been observed which can be attributed to the adsorption of K<sub>4</sub>[Fe(CN)<sub>6</sub>] on the hematite surface. By comparing the slopes, it was found that the electroactive surface area of Ba- and Sr-modified hematite electrodes is 2.4 and 3.2 times higher than that of bare hematite. These values are in well-agreement with the observed enhancement in the photocurrent and with SEM observations, however, the electroactive surface area was measured in the dark indicating that the electroactive surface area plays a crucial role. To investigate the stability of the Ba- and Sr-modified hematite photoanodes, chronoamperometry curves were measured for approximately 3 h under

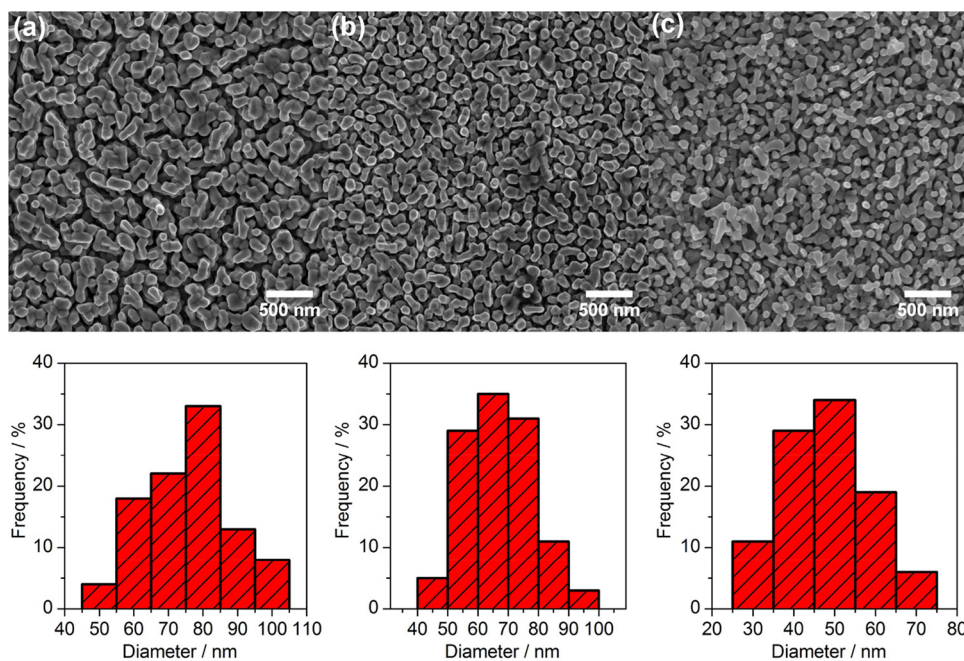


**Fig. 2.** SEM images and particle size distribution histograms of (a) bare hematite, (b) Ba-modified hematite, and (c) Sr-modified hematite films.

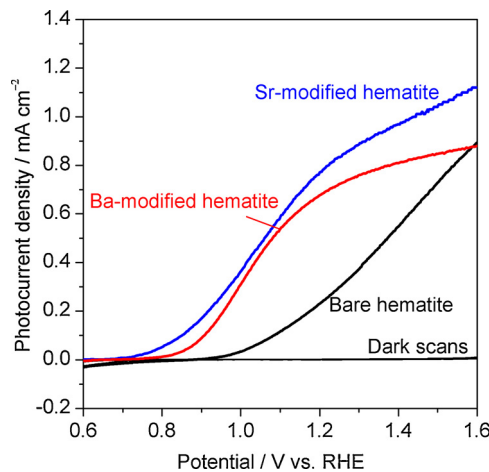


**Fig. 3.** I-V curves for photoelectrochemical water oxidation on bare hematite and on Ba- and Sr-modified hematite photoanodes measured under simulated solar light (1 sun, AM 1.5 G) in 1.0 M NaOH aqueous solution.

standard illumination conditions from 1.0 M NaOH solution at 1.23 V vs. RHE and presented in Fig. S6. Both photoanodes exhibit stable photocurrent evincing their stability.

### 3.3. Spectroscopic measurements

#### 3.3.1. EIS and PEIS measurements

In order to disclose whether the cathodic shift in the onset potential of the photocurrent is due to the shift in the flat-band potential or not, the flat-band potential of bare hematite and of Ba- and Sr-modified hematite photoanodes was determined by using Mott-Schottky (M-S) equation [40]:

$$\frac{1}{C^2} = \frac{2}{\varepsilon \varepsilon_0 q N_D A^2} \left( E - E_{FB} - \frac{k_B T}{q} \right)$$

where C is the capacitance of the space charge layer,  $\varepsilon$  is the dielectric constant (80 for hematite) [41],  $\varepsilon_0$  the vacuum permittivity

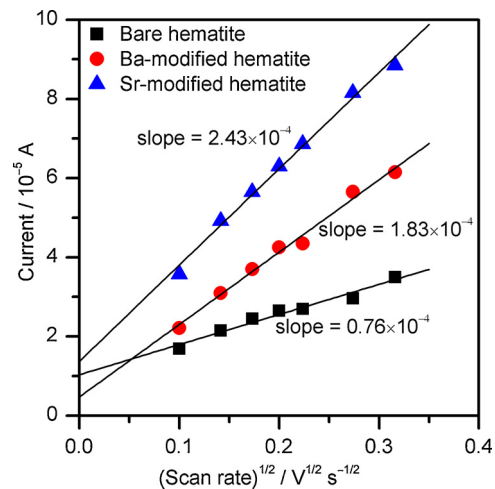


**Fig. 4.** Relationship between the peak current and the scan rate square root fitted by Randles-Sevcik equation for bare hematite and for Ba- and Sr-modified hematite electrodes.

$(8.85 \times 10^{-14} F cm^{-1})$ , A is the area of the electrode exposed to the electrolyte,  $N_D$  is the donor density, E the applied potential,  $E_{FB}$  is the flat band potential, q is the elementary charge ( $1.6 \times 10^{-19} C$ ),  $k_B$  is the Boltzmann's constant ( $1.38 \times 10^{-23} J K^{-1}$ ), and T is the absolute temperature (298 K). According to the M-S equation, the flat-band potential can be determined from the intercept of the M-S plot. As shown in Fig. 5, good straight lines were obtained as predicted by the M-S equations and the flat-band potentials of bare hematite and of Ba- and Sr-modified hematite electrodes are the same. Accordingly, the possibility that the cathodic shift in the onset potential of the photocurrent (Fig. 3) is attributed to the shift in the flat-band potential can be omitted.

It is worth mentioning that however the M-S plot can be used to determine the flat-band potential in a relatively accurate way, the determination of the donor density is questionable as the capacitance often depend on the frequency. This is due to the presence of surface irregularities and/or surface states [42]. Thus, the donor density was

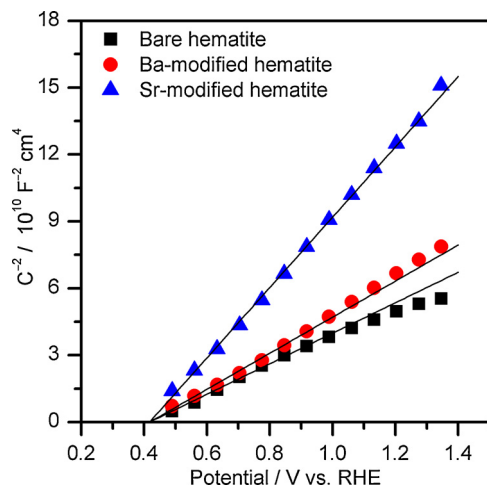


**Fig. 5.** Mott-Schottky plots of bare hematite and of Ba- and Sr-modified hematite photoanodes measured at 1.0 kHz in the dark, electrolyte 1.0 M NaOH aqueous solution.

calculated from the slope of M-S plot measured at high frequency to avoid the contribution from the surface state and double layer capacitances. The results indicated that the donor densities of Ba- and Sr-modified hematite electrodes are  $1.99 \times 10^{19}$  and  $1.12 \times 10^{19} \text{ cm}^{-3}$ , respectively. They are lower than that of bare hematite (i.e.,  $2.58 \times 10^{19} \text{ cm}^{-3}$ ). This again indicates that  $\text{Ba}^{2+}$  and  $\text{Sr}^{2+}$  ions are more likely not doped into the hematite structure, rather, they most likely act as a morphology-directing agents. It is worth also mentioning that the morphology of the films might affect the slope of M-S plot, however this effect is diminished at high donor density values as previously reported [43,44].

To explore the role of the surface states, the photoelectrochemical impedance spectroscopy (PEIS) technique has been employed to measure the capacitance of surface states. In fact, the capacitance of surface states ( $C_{ss}$ ) has recently been used to characterize the energy distribution and the density of surface states [45,46]. Fig. S7 shows the typical Nyquist plots obtained for bare hematite and for Ba- and Sr-modified hematite photoanodes measured at different applied potentials. For clarity, few spectra have been presented in Fig. S7; however, the potential interval was 25 mV. For comparison, Fig. 6a represents the Nyquist plot of bare hematite and of Ba- and Sr-modified hematite

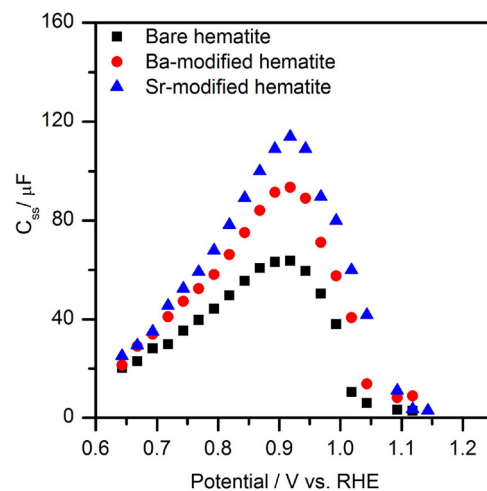


**Fig. 7.** Surface-state capacitance  $C_{ss}$  calculated by fitting the equivalent circle presented in Fig. 6b to the Nyquist plots obtained from PEIS measurements of bare hematite and of Ba- and Sr-modified hematite photoanodes at different applied potentials.

photoanodes measured at 0.97 V vs RHE. For all electrodes, two semicircles were observed, the one at the high frequencies is attributed to the electrochemical processes in the bulk of the semiconductor electrode whereas the semicircle at low frequencies describes the electrochemical processes occur at the surface [45]. By fitting the PEIS spectra with the equivalent circuit (EC) presented in Fig. 6b, the capacitance associated with surface states  $C_{ss}$  in addition to the other impedance parameters (e.g. the series resistance  $R_s$ , the space-charge layer capacitance  $C_{bulk}$ , the bulk charge trapping resistance  $R_{trap}$ , and the charge transfer resistance across the hematite/electrolyte interface,  $R_{ct}$ ) have been obtained [45,46]. By plotting the  $C_{ss}$  against the applied potential (Fig. 7), it was found that all photoanodes exhibit a characteristic peak which is typically found in the system when the oxygen evolution reaction (OER) proceeds via surface states [38,45,46]. By integrating the area under the peaks, the total charge in the surface states can be semi-quantitatively determined. It was found that the amount of the charge in the surface states of Ba- and Sr-modified hematite photoanodes are 1.45 and 1.8 times higher than that of bare hematite. However, it is commonly proposed that the surface states can act as recombination centers and their passivation is required to enhance the photoactivity of

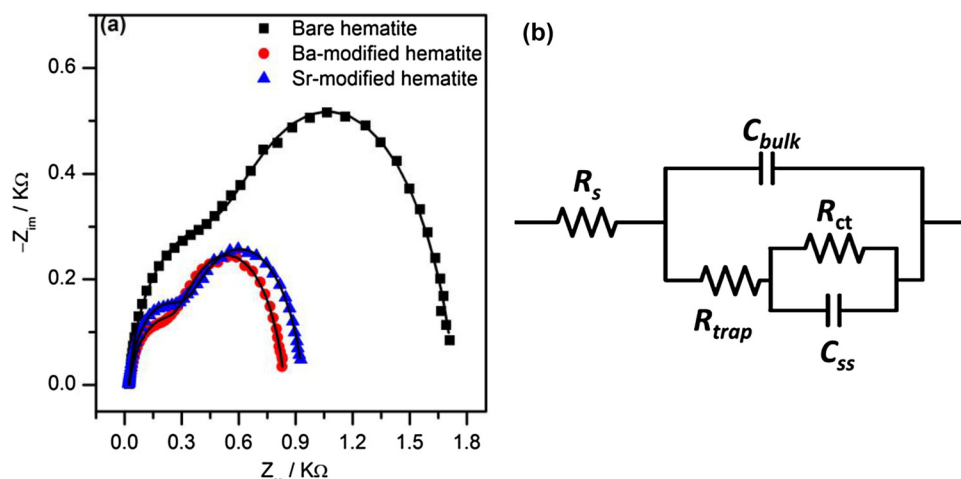


**Fig. 6.** (a) Nyquist plot of bare hematite and of Ba- and Sr-modified hematite photoanodes measured under illumination at 0.97 V vs. RHE. Electrolyte (1.0 M NaOH aqueous solution), light intensity (1 sun, AM 1.5 G). (b) Equivalent circuit used for fitting the PEIS spectra.

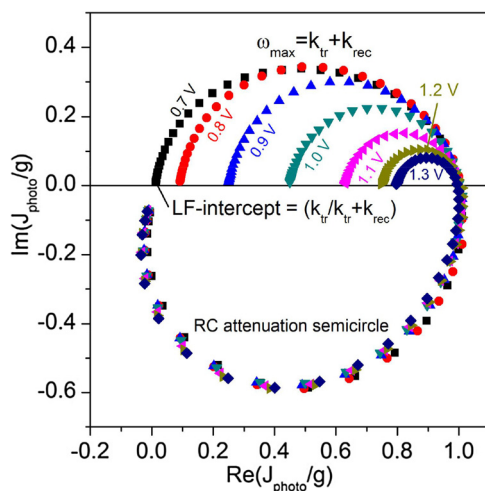


**Fig. 8.** Normalized IMPS responses of Sr-modified hematite photoanode measured at different applied potentials versus RHE. Electrolyte (1.0 M NaOH aqueous solution), light intensity ( $52 \text{ mW cm}^{-2}$ , monochromatic 470 nm).

hematite [24], it was recently demonstrated that the surface states might also acts as catalytic centers for water oxidation [46]. Specially, under illumination where the Fermi level of hematite will split into quasi Fermi level of electron and hole due to the electron/hole pairs generation in the space charge layer. With increasing the bias potential, the Fermi level of the hole shifts downward gradually until reaches the energy level of the surface states. Then, the surface states turned vacant and activated to catalyze water oxidation by accommodating the donated electrons. Thus, the higher density of surface states might be the reason for the higher photocurrent observed for Ba- and Sr-modified hematite photoanodes at low bias potential and thus it might explain the cathodic shift in the onset potential of the photocurrent (Fig. 3). The M-S plots for bare hematite and Ba- and Sr-modified photoanodes were again constructed by using the  $C_{\text{bulk}}$  obtained from the fitting of the EIS spectra (Fig. S8). The donor densities were calculated from the slopes and it was found that the donor densities for Ba- and Sr-modified hematite photoanode are  $1.23 \times 10^{19}$  and  $1.94 \times 10^{19} \text{ cm}^{-3}$ , respectively, while the donor density of bare hematite photoanode is  $1.93 \times 10^{19} \text{ cm}^{-3}$ . These values are close to that calculated from the M-S plots measured in the dark evincing the validity of the obtained results.

### 3.3.2. IMPS measurements

To further elucidate the role of the surface states in enhancing the photocurrent of the modified hematite electrodes, the kinetics of hole-electron pair recombination and transfer at the hematite/electrolyte interface have been studied by IMPS [22,47–49]. Fig. 8 depicts the typical IMPS responses for Sr-modified hematite photoanode. The IMPS responses of bare hematite and of Ba-modified hematite photoanodes are also presented in Figs. S9 and S10, respectively. The high frequency semicircle in the low quadrant corresponds to the RC attenuation of the IMPS response with the time constant  $R_{\text{series}}C_{\text{sc}}$ . The semicircle in the upper quadrant at low frequency is due to the competition between interfacial charge transfer and recombination [50]. The rate constant of charge recombination ( $k_{\text{rec}}$ ) and charge transfer ( $k_{\text{tr}}$ ) can thus be derived from the low frequency semicircle maximum occurs at the radial frequency ( $\omega_{\text{max}} = k_{\text{tr}} + k_{\text{rec}}$ ) and from the low-frequency intercept (LF-intercept) ( $= k_{\text{tr}}/k_{\text{tr}} + k_{\text{rec}}$ ) of the normalized IMPS response as illustrated in Fig. 8 [51]. It is clear from the calculated recombination rate constant presented in Fig. 9a that the surface electron-hole recombination has prominently suppressed for both Ba- and Sr-modified hematite. Meanwhile, the rate constants of interfacial charge transfer have been improved in particular for Sr-modified hematite which is consistent with the observed photocurrent responses and the assumption that the surface states enhance the water oxidation at low bias potential. However it is commonly believed that the surface states act as a recombination centres [24], it seems that they also act as an active sites for water oxidation and facilitate the charge transfer [46].

## 4. Conclusions

In conclusion, hematite photoanodes with size-controlled nanoparticles were synthesized via a simple chemical bath deposition method at low temperature (95 °C) using  $\text{Ba}^{2+}$  and  $\text{Sr}^{2+}$  ions as morphology-directing agents. The average diameter of hematite particles decreased by a factor of 13% and 35% upon addition of  $\text{Ba}^{2+}$  and  $\text{Sr}^{2+}$  ions into the chemical bath, respectively, in comparison with that of bare hematite. Consequently, the electroactive surface area of Ba- and Sr-modified hematite electrodes increased by 2.4 and 3.2 times, respectively, as concluded from the cyclic voltammetry measurements. As a result, the generated photocurrent at 1.23 V vs. RHE under standard illumination conditions on Ba- and Sr-modified hematite photoanodes increased by 2.6 and 3 times, respectively, in comparison with that of bare hematite. The photocurrent onset potential for water oxidation on Ba- and Sr-modified hematite photoanodes was cathodically shifted by

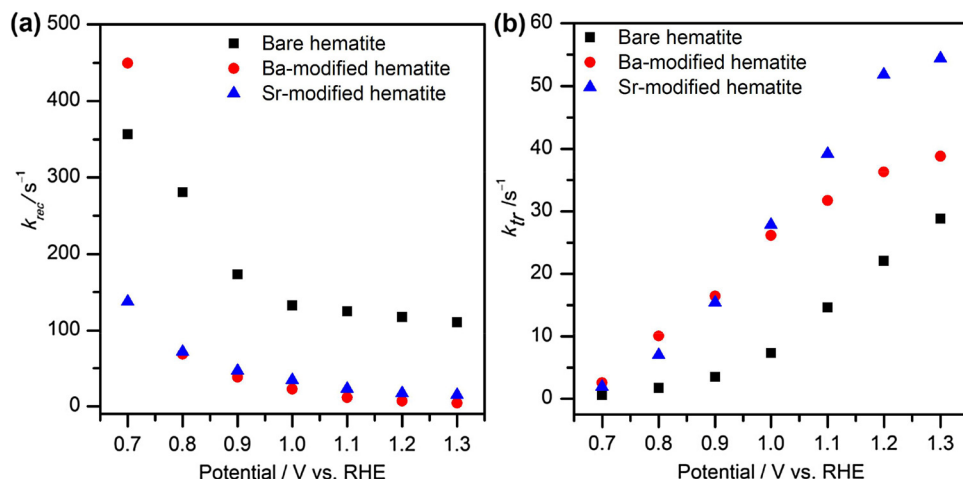


**Fig. 9.** Rate constant of (a) charge recombination ( $k_{\text{rec}}$ ) and (b) charge transfer for bare hematite and for Ba-, and Sr-modified hematite photoanodes at different applied potentials.

about 150 and 220 mV, respectively, relative to that on bare hematite. The photocurrent enhancement can readily be attributed to the enhanced electroactive surface area as it can be seen from the good correlation between both of them. However, the cathodic shift in the photocurrent onset potential was elucidated based on the density of surface states and on the rate constants of surface charge transfer and recombination measured by PEIS and IMPS, respectively. Ba- and Sr-modified hematite photoanodes exhibit higher density of surface states and higher charge transfer rate constants at low bias potential than that of bare hematite. They also exhibit lower charge recombination rate constants at low bias potential than that of bare hematite. Accordingly, the water oxidation at low bias potential is faster on Ba- and Sr-modified hematite photoanodes than on bare hematite and thus they have a higher photocurrent and a lower onset potential for water oxidation.

## Acknowledgments

The authors acknowledge the financial from the Science and Technology Development Fund (STDF, GERC III, Project ID 5064). T. A. K acknowledges the support provided by the Deanship of Scientific Research (DSR) at King Fahd University of Petroleum & Minerals (KFUPM) through the project No. SR161020.

## Appendix A. Supporting information

Supplementary data associated with this article can be found in the online version

## Appendix B. Supplementary data

Supplementary material related to this article can be found, in the online version, at doi:<https://doi.org/10.1016/j.apcatb.2018.04.073>.

## References

- [1] J.R. McKone, N.S. Lewis, H.B. Gray, Will solar-driven water-splitting devices see the light of day? *Chem. Mater.* 26 (2014) 407–414.
- [2] Z. Zhang, P. Wang, Optimization of photoelectrochemical water splitting performance on hierarchical TiO<sub>2</sub> nanotube arrays, *Energy Environ. Sci.* 5 (2012) 6506–6512.
- [3] L. Zhang, C.-Y. Lin, V.K. Valev, E. Reisner, U. Steiner, J.J. Baumberg, Plasmonic enhancement in BiVO<sub>4</sub> photonic crystals for efficient water splitting, *Small* 10 (2014) 3970–3978.
- [4] X. Liu, F. Wang, Q. Wang, Nanostructure-based WO<sub>3</sub> photoanodes for photoelectrochemical water splitting, *Phys. Chem. Chem. Phys.* 14 (2012) 7894–7911.
- [5] L. Zhang, D. Bahnemann, Synthesis of nanovoid Bi<sub>2</sub>WO<sub>6</sub> 2D ordered arrays as photoanodes for photoelectrochemical water splitting, *ChemSusChem* 6 (2013) 283–290.
- [6] M. Higashi, K. Domen, R. Abe, Highly stable water splitting on oxynitride TaON photoanode system under visible light irradiation, *J. Am. Chem. Soc.* 134 (2012) 6968–6971.
- [7] M. Higashi, K. Domen, R. Abe, Fabrication of an efficient BaTaO<sub>2</sub>N photoanode harvesting a wide range of visible light for water splitting, *J. Am. Chem. Soc.* 135 (2013) 10238–10241.
- [8] C.-Y. Lin, Y.-H. Lai, D. Mersch, E. Reisner, Cu<sub>2</sub>O|NiO<sub>x</sub> nanocomposite as an inexpensive photocathode in photoelectrochemical water splitting, *Chem. Sci.* 3 (2012) 3482–3487.
- [9] S. Ida, K. Yamada, T. Matsunaga, H. Hagiwara, Y. Matsumoto, T. Ishihara, Preparation of p-type CaFe<sub>2</sub>O<sub>4</sub> photocathodes for producing hydrogen from water, *J. Am. Chem. Soc.* 132 (2010) 17343–17345.
- [10] M.P. Dare-Edwards, J.B. Goodenough, A. Hamnett, P.R. Trevellick, Electrochemistry and photoelectrochemistry of iron(III) oxide, *J. Chem. Soc. Faraday Trans. 1* 79 (1983) 2027–2041.
- [11] F.J. Morin, Electrical properties of α-ferric oxide, *Phys. Rev.* 93 (1954) 1195–1199.
- [12] J.H. Kennedy, K.W. Frese, Photooxidation of water at α-Fe<sub>2</sub>O<sub>3</sub> electrodes, *J. Electrochem. Soc.* 125 (1978) 709–714.
- [13] Y. Lin, Y. Xu, M.T. Mayer, Z.L. Simpson, G. McMahon, S. Zhou, D. Wang, Growth of p-type hematite by atomic layer deposition and its utilization for improved solar water splitting, *J. Am. Chem. Soc.* 134 (2012) 5508–5511.
- [14] X. Qi, G. She, M. Wang, L. Mu, W. Shi, Electrochemical synthesis of p-type Zn-doped α-Fe<sub>2</sub>O<sub>3</sub> nanotube arrays for photoelectrochemical water splitting, *Chem. Commun.* 49 (2013) 5742–5744.
- [15] I. Cesar, A. Kay, J.A.G. Martinez, M. Grätzel, Translucent thin film Fe<sub>2</sub>O<sub>3</sub> photoanodes for efficient water splitting by sunlight: nanostructure-directing effect of Si-doping, *J. Am. Chem. Soc.* 128 (2006) 4582–4583.
- [16] G. Wang, Y. Ling, D.A. Wheeler, K.E.N. George, K. Horsley, C. Heske, J.Z. Zhang, Y. Li, Facile synthesis of highly photoactive α-Fe<sub>2</sub>O<sub>3</sub>-based films for water oxidation, *Nano Lett.* 11 (2011) 3503–3509.
- [17] Y.C. Ling, G.M. Wang, D.A. Wheeler, J.Z. Zhang, Y. Li, Sn-doped hematite nanostructures for photoelectrochemical water splitting, *Nano Lett.* 11 (2011) 2119–2125.
- [18] A.G. Tamirat, W.-N. Su, A.A. Dubale, H.-M. Chen, B.-J. Hwang, Photoelectrochemical water splitting at low applied potential using a NiOOH coated codoped (Sn, Zr) α-Fe<sub>2</sub>O<sub>3</sub> photoanode, *J. Mater. Chem. A* 3 (2015) 5949–5961.
- [19] R. Zhang, L. Yang, X. Huang, T. Chen, F. Qu, Z. Liu, G. Du, A.M. Asiri, X. Sun, Se doping: an effective strategy toward Fe<sub>2</sub>O<sub>3</sub> nanorod arrays for greatly enhanced solar water oxidation, *J. Mater. Chem. A* 5 (2017) 12086–12090.
- [20] X. Huang, L. Yang, S. Hao, B. Zheng, L. Yan, F. Qu, A.M. Asiri, X. Sun, N-Doped carbon dots: a metal-free co-catalyst on hematite nanorod arrays toward efficient photoelectrochemical water oxidation, *Inorg. Chem. Front.* 4 (2017) 537–540.
- [21] R. Zhang, Y. Fang, T. Chen, F. Qu, Z. Liu, G. Du, A.M. Asiri, T. Gao, X. Sun, Enhanced photoelectrochemical water oxidation performance of Fe<sub>2</sub>O<sub>3</sub> nanorods array by S doping, *ACS Sustain. Chem. Eng.* 5 (2017) 7502–7506.
- [22] M.G. Ahmed, I.E. Kretschmer, T.A. Kandiel, A.Y. Ahmed, F.A. Rashwan, D.W. Bahnemann, A facile surface passivation of hematite photoanodes with TiO<sub>2</sub> overlayers for efficient solar water splitting, *ACS Appl. Mater. Interfaces* 7 (2015) 24053–24062.
- [23] D.K. Zhong, M. Cornuz, K. Sivula, M. Grätzel, D.R. Gamelin, Photo-assisted electrodeposition of cobalt-phosphate (Co-Pi) catalyst on hematite photoanodes for solar water oxidation, *Energy Environ. Sci.* 4 (2011) 1759–1764.
- [24] F. Le Formal, N. Tetreault, M. Cornuz, T. Moehl, M. Grätzel, K. Sivula, Passivating surface states on water splitting hematite photoanodes with alumina overlayers, *Chem. Sci.* 2 (2011) 737–743.
- [25] J. Li, F. Meng, S. Suri, W. Ding, F. Huang, N. Wu, Photoelectrochemical performance enhanced by a nickel oxide-hematite p-n junction photoanode, *Chem. Commun.* 48 (2012) 8213–8215.
- [26] M.G. Ahmed, T.A. Kandiel, A.Y. Ahmed, I. Kretschmer, F. Rashwan, D. Bahnemann, Enhanced photoelectrochemical water oxidation on nanostructured hematite photoanodes via p-CaFe<sub>2</sub>O<sub>4</sub>/n-Fe<sub>2</sub>O<sub>3</sub> heterojunction formation, *J. Phys. Chem. C* 119 (2015) 5864–5871.
- [27] S. Liu, L. Zheng, P. Yu, S. Han, X. Fang, Novel composites of α-Fe<sub>2</sub>O<sub>3</sub> tetra-kaidecahedron and graphene oxide as an effective photoelectrode with enhanced photocurrent performances, *Adv. Funct. Mater.* 26 (2016) 3331–3339.
- [28] I. Kondofersky, H.K. Dunn, A. Müller, B. Mandlmeier, J.M. Feckl, D. Fattakhova-Rohlfing, C. Scheu, L.M. Peter, T. Bein, Electron collection in host–guest nanostructured hematite photoanodes for water splitting: the influence of scaffold doping density, *ACS Appl. Mater. Interfaces* 7 (2015) 4623–4630.
- [29] C. Ding, Z. Wang, J. Shi, T. Yao, A. Li, P. Yan, B. Huang, C. Li, Substrate–electrode interface engineering by an electron-transport layer in hematite photoanode, *ACS Appl. Mater. Interfaces* 8 (2016) 7086–7091.
- [30] A. Iwase, H. Kato, A. Kudo, The effect of alkaline earth metal ion dopants on photocatalytic water splitting by NaTaO<sub>3</sub> powder, *ChemSusChem* 2 (2009) 873–877.
- [31] Y. Li, L. Zhang, A. Torres-Pardo, J.M. González-Calbet, Y. Ma, P. Oleynikov, O. Terasaki, S. Asahina, M. Shima, D. Cha, L. Zhao, K. Takanabe, J. Kubota, K. Domen, Cobalt phosphate-modified barium-doped tantalum nitride nanorod photoanode with 1.5% solar energy conversion efficiency, *Nat. Commun.* 4 (2013).
- [32] J. Zhao, H.-S. Chen, K. Matras-Postolek, P. Yang, Morphology evolution of α-Fe<sub>2</sub>O<sub>3</sub> controlled via incorporation of alkaline earth metal ions, *CrystEngComm* 17 (2015) 7175–7181.
- [33] Z. Guo, C. Li, W. Li, H. Guo, X. Su, P. He, Y. Wang, Y. Xia, Ruthenium oxide coated ordered mesoporous carbon nanofiber arrays: a highly bifunctional oxygen electrocatalyst for rechargeable Zn-air batteries, *J. Mater. Chem. A* 4 (2016) 6282–6289.
- [34] A. Kay, I. Cesar, M. Grätzel, New benchmark for water photooxidation by nanostructured α-Fe<sub>2</sub>O<sub>3</sub> films, *J. Am. Chem. Soc.* 128 (2006) 15714–15721.
- [35] J.A. Dean, Lange's Handbook of Chemistry, McGRAW-HILL, INC., 1999.
- [36] N. Beermann, L. Vayssières, S.E. Lindquist, A. Hagfeldt, Photoelectrochemical studies of oriented nanorod thin films of hematite, *J. Electrochem. Soc.* 147 (2000) 2456–2461.
- [37] Y.-S. Hu, A. Kleiman-Shwarzstein, G.D. Stucky, E.W. McFarland, Improved photoelectrochemical performance of Ti-doped α-Fe<sub>2</sub>O<sub>3</sub> thin films by surface modification with fluoride, *Chem. Commun.* (2009) 2652–2654.
- [38] B. Klahr, S. Gimenez, F. Fabregat-Santiago, T. Hamann, J. Bisquert, Water oxidation at hematite photoelectrodes: the role of surface states, *J. Am. Chem. Soc.* 134 (2012) 4294–4302.
- [39] A.J. Bard, L.R. Faulkner, Electrochemical Methods Fundamentals and Applications, JOHN WILEY & SONS, INC., 2001.
- [40] G. Cooper, J.A. Turner, A.J. Nozik, Mott-Schottky plots and flat-band potentials for single-crystal rutile electrodes, *J. Electrochem. Soc.* 129 (1982) 1973–1977.
- [41] J.H. Kennedy, K.W. Frese, Flatband potentials and donor densities of polycrystalline α-Fe<sub>2</sub>O<sub>3</sub> determined from Mott-Schottky plots, *J. Electrochem. Soc.* 125 (1978) 723–726.
- [42] Z. Chen, T. Deutsch, H. Dinh, K. Domen, K. Emery, A. Forman, N. Gaillard,

- R. Garland, C. Heske, T. Jaramillo, A. Kleiman-Shwarscstein, E. Miller, K. Takanabe, J. Turner, *Photoelectrochemical Water Splitting: Standards, Experimental Methods, and Protocols*, Photoelectrochemical Water Splitting, Springer, New York, 2013, pp. 7–16.
- [43] I. Mora-Seró, F. Fabregat-Santiago, B. Denier, J. Bisquert, R. Tena-Zaera, J. Elias, C. Lévy-Clément, Determination of carrier density of ZnO nanowires by electrochemical techniques, *Appl. Phys. Lett.* 89 (2006) 203117.
- [44] J. Bisquert, G. García-Belmonte, F. Fabregat-Santiago, Modelling the electric potential distribution in the dark in nanoporous semiconductor electrodes, *J. Solid State Electrochem.* 3 (1999) 337–347.
- [45] B. Iandolo, A. Hellman, The role of surface states in the oxygen evolution reaction on hematite, *Angew. Chem.- Int. Ed.* 53 (2014) 13404–13408.
- [46] Z. Wang, F. Fan, S. Wang, C. Ding, Y. Zhao, C. Li, Bridging surface states and current-potential response over hematite-based photoelectrochemical water oxidation, *RSC Adv.* 6 (2016) 85582.
- [47] L.M. Peter, Energetics and kinetics of light-driven oxygen evolution at semiconductor electrodes: the example of hematite, *J. Solid State Electrochem.* 17 (2013) 315–326.
- [48] L.M. Peter, K.G.U. Wijayantha, A.A. Tahir, Kinetics of light-driven oxygen evolution at  $\alpha\text{-Fe}_2\text{O}_3$  electrodes, *Faraday Discuss.* 155 (2012) 309–322.
- [49] A.Y. Ahmed, M.G. Ahmed, T.A. Kandiel, Modification of hematite photoanode with cobalt based oxygen evolution catalyst via bifunctional linker approach for efficient water splitting, *J. Phys. Chem. C* 120 (2016) 23415–23420.
- [50] H.K. Dunn, J.M. Feckl, A. Muller, D. Fattakhova-Rohlfing, S.G. Morehead, J. Roos, L.M. Peter, C. Scheu, T. Bein, Tin doping speeds up hole transfer during light-driven water oxidation at hematite photoanodes, *Phys. Chem. Chem. Phys.* 16 (2014) 24610–24620.
- [51] L. Peter, Kinetics and mechanisms of light-driven reactions at semiconductor electrodes: principles and techniques, in: H.-J. Lewerenz, L. Peter (Eds.), *Photoelectrochemical Water Splitting: Materials, Processes and Architectures*, The Royal Society of Chemistry, 2013 Chapter 2, pp. 19–51.